

1                   **The effect of faceting on olivine wetting properties**

2                   Yongsheng Huang<sup>1\*</sup>,<sup>a</sup>, Takayuki Nakatani<sup>1,b</sup>, Sando Sawa<sup>1,c</sup>, Michihiko Nakamura<sup>1</sup>, Catherine

3                   McCammon<sup>2</sup>

4                   *1. Department of Earth Science, Graduate School of Science, Tohoku University, Aramaki–Aza–*  
5                   *Aoba, Aoba–Ku, Sendai, Miyagi 980–8578, Japan*

6                   *2. Bayerisches Geoinstitut, University of Bayreuth, 95440 Bayreuth, Germany*

7                   *a. Current address: Guangzhou Institute of Geochemistry, Chinese Academy of Sciences, 511*  
8                   *Kehua Street, Wushan, Tianhe, Guangzhou 510640, China.*

9                   *b. Current address: Geological Survey of Japan, AIST Central 7, Higashi 1–1–1, Tsukuba,*  
10                  *Ibaraki 305–8567, Japan.*

11                  *c. Current address: Division of Advanced Mechanical Systems Engineering, Institute of*  
12                  *Engineering, Tokyo University of Agriculture and Technology, Nakamachi 2-24-16, Koganei,*  
13                  *Tokyo, 184-0012, Japan.*

14                  \* Corresponding author. Email: huangyongsheng@gig.ac.cn

15

16                  **Key points**

- 17                  1. Faceting produces larger dihedral angles than those with curved interfaces in the olivine–  
18                  fluid system.
- 19                  2. Grain boundary planes are frequently composed of low–index planes, and the facet–facet  
20                  angles are explained by olivine crystallography.
- 21                  3. The facet proportion is consistent with electrical conductivity data; faceting effects could  
22                  be magnified under a sheared-wedge mantle.

26     **Abstract**

27                 Grain-scale pore geometry primarily controls the fluid distribution in rocks, affecting  
28     material transport and geophysical response. The dihedral angle ( $\theta$ ) in the olivine–fluid system is  
29     a key parameter determining the pore fluid geometry in mantle wedges. Both curved and faceted  
30     olivine–fluid interfaces define  $\theta$  in the system, generating the faceted–faceted (FF), faceted–curved  
31     (FC), and curved–curved (CC) angles. However, the effect of faceting on  $\theta$  under various pressure  
32     and temperature (P–T) conditions and fluid compositions have not been constrained, and its  
33     mineralogical understanding is unresolved. This study evaluates the facet-bearing  $\theta$  and their  
34     proportions in olivine–multicomponent aqueous fluid systems. Our results show that 1/3 of  
35     olivine–fluid  $\theta$  are facet-bearing angles irrelative to the P–T conditions and fluid compositions.  
36     Faceting produces larger dihedral angles than the CC angles. The grain boundary plane (GBP)  
37     distribution reveals that the GBPs of faceted interfaces at triple junctions were subjected to low  
38     Miller Index faces ((100), (010), and (101)). Moreover, calculating the FF angles from two  
39     adjacent low Miller index planes highly reproduces measured angle values based on the olivine  
40     crystal habit. Therefore, our study suggests that the FF angle is strongly affected by olivine  
41     crystallography. The presence of faceting increases  $\theta$  and critical fluid fraction ( $\phi_c$ ) for percolation,  
42     thus decreases the permeability. In the mantle wedge, where olivine crystallographic preferred  
43     orientation (CPO) is expected, increasing the FF angle proportion with associated changes in fluid  
44     pore morphology will lead to the permeability anisotropy and consequent geophysical anomalies.

45

46

47 **Plain Language Summary**

48 Pore geometry controls fluid-bearing rocks' material transport and geophysical properties,  
49 affecting elemental cycling and the interpretation of magnetotelluric and seismological  
50 observations in subduction zones. The dihedral angle ( $\theta$ ) in the olivine–fluid system is a key  
51 parameter determining fluid geometry in a mantle wedge. Both curved and faceted olivine–fluid  
52 interfaces appear, but the effect of faceting on  $\theta$  under various P–T conditions and fluid  
53 compositions is poorly constrained. Here, we measured the facet-bearing  $\theta$  and their proportions  
54 in olivine–multicomponent aqueous fluid systems. The results show that 1/3 of olivine–fluid  $\theta$  are  
55 facet-bearing irrelative of the P–T conditions and fluid compositions. The  $\theta$  values of the facet–  
56 bearing angle are comparable to, or larger than, the curved–curved angle. Both grain boundary  
57 planes of faceted olivine–fluid interfaces are preferentially subjected to low Miller Index faces;  
58 thus, the FF angle is strongly affected by olivine crystallography. The presence of faceting  
59 increases  $\theta$ , the critical fluid fraction ( $\phi_c$ ), and decreases the permeability. In the mantle wedge,  
60 where olivine crystallographic preferred orientation (CPO) is expected, the presence of an FF angle  
61 with associated changes in fluid pore morphology will lead to permeability anisotropy and  
62 geophysical anomalies.

63 **Key words:** dihedral angle, faceted plane, Miller Index, crystallographic orientation, fluid  
64 connectivity, permeability anisotropy.

65

66

67

68     **1. Introduction**

69              Pore geometry significantly controls the distribution of geological fluid (i.e., aqueous fluid  
70          and silicate melt) in a deep mantle wedge, thereby affecting element cycling and geophysical  
71          response in subduction zones (Watson & Brenan, 1987; Hermann et al., 2006; Iwamori, 1998; van  
72          Keeken et al., 2011; Pommier & Evans, 2017; Worzewski et al., 2011; Zheng et al., 2016). Although  
73          channelized fluid flow has often been inferred from the field studies (Angiboust et al., 2014), the  
74          pervasive grain-scale fluid flow may be the most plausible fluid migration regime at high pressure  
75          (P) and high temperature (T) conditions where dissolution-precipitation intensively operates and  
76          interfacial energy minimization (“textural equilibrium”) is quickly attained. Moreover, the  
77          pervasive nature may be suitable for explaining the resistivity anomalies observed at a  
78          magnetotelluric (MT) grid-scale (commonly  $>10$  km), because it would be required for the  
79          channelized flows to be distributed continuously and nearly isotropically over this length scale. In  
80          an olivine-dominant mantle rock, the olivine–fluid dihedral angle ( $\theta$ ) is the primary parameter  
81          controlling the grain-scale fluid connectivity (Huang et al., 2019, 2020; Mibe et al., 1999;  
82          Toramaru & Fujii, 1986). Therefore, a precise constraint on  $\theta$  in the olivine–fluid system is  
83          important for a complete understanding of the fluid distribution and migration in subduction zones.

84              The dihedral angle is a consequence of the fluid–mineral interaction, which changes the  
85          fluid pore geometry through dissolution and precipitation processes to minimize the interfacial  
86          energy in the system. It is defined as the ratio of the grain boundary energy ( $\gamma_{ss}$ ) to the solid–fluid  
87          interfacial energy ( $\gamma_{sf}$ ) (von Bargen & Waff, 1986; Watson & Brenan, 1987) as follows:

88              
$$2 \cos(\theta/2) = \gamma_{ss}/\gamma_{sf} \quad (1).$$

89 In an isotropic system, where solid–fluid interfaces are smoothly curved with a constant mean  
90 curvature, the geometry of the intergranular fluid is solely determined by the dihedral angle. Fluids  
91 can wet the grain edges well and migrate along with interconnected tubular networks at  $\theta < 60^\circ$   
92 irrespective of the fluid fraction ( $\phi$ ). In contrast, the fluid is distributed as isolated pockets along  
93 the grain edges, corners, and boundaries at  $\theta > 60^\circ$  when  $\phi$  is lower than the critical value ( $\phi_c$ )  
94 (Watson & Brenan, 1987; Holness, 1992, 1993), which is dependent on  $\theta$  (von Bargen & Waff,  
95 1986). However, the fluid distribution in the realistic rocks can deviate from the ideal distribution  
96 (Laporte & Watson, 1995; Waff & Faul, 1992). In fact, Huang et al. (2021) measured the electrical  
97 conductivity of the texturally equilibrated forsterite–saline fluid aggregate at 800°C and 1 GPa  
98 showing that the conductivity is significantly smaller than that expected from the interconnected  
99 tube model especially at low  $\phi$ . The synchrotron X–ray microtomography (CT) of the post-run  
100 products revealed that the fluid pores gradually get interconnected with each other, increasing  $\phi$   
101 above ~1.0 % even though  $\theta$  defined by the curved–curved interface is smaller than 60° under the  
102 experimental conditions (Huang et al., 2019).

103 In a realistic mineral–fluid system with interfacial energy anisotropy, facet planes,  
104 crystallographically controlled planar solid–liquid interfaces, are often present along with the  
105 curved interface (Watson & Lupulescu, 1993; Price et al., 2006; Wark & Watson, 2000; Watson,  
106 1999). The coexistence of both curved and faceted interfaces generates three types of  $\theta$ : curved–  
107 curved (CC), faceted–curved (FC), and faceted–faceted (FF)  $\theta$  (Yoshino et al., 2006). Pores  
108 surrounded by facet planes are difficult to connect unless  $\phi$  increase above the critical value which  
109 depends on  $\theta$  defined by the faceted interfaces (Price et al., 2006). Therefore, the facet plane may  
110 affect the fluid connectivity depending on its  $\theta$  values, which helps to explain the results of

111 electrical conductivity measurements in Huang et al. (2021). Price et al. (2006) reported that facet  
112 bearing angles are larger than those of the curved–curved interfaces in the quartz–fluid and  
113 tremolite–fluid systems. If this is the case, facet-bearing pores may require the relatively high  $\phi$   
114 for the fluid interconnection. Although many studies have been conducted to investigate the P–T,  
115 fluid composition, and mineral assemblage dependence of  $\theta$  in the olivine–fluid system (Watson  
116 & Brenan, 1987; Huang et al., 2019, 2020; Mibe et al., 1998, 1999; Yoshino et al., 2006), the effect  
117 of the angle-type variation on  $\theta$  is poorly understood. Yoshino et al. (2006) systematically  
118 investigated the effect of faceting on pore geometry in texturally equilibrated rocks and discussed  
119 its implications for permeability in several representative systems, including the San Carlos  
120 olivine–MORB melt. However, olivine (forsterite)–aqueous fluid systems have not yet been  
121 studied. Huang et al. (2019, 2020) studied the dihedral angle between olivine and multicomponent  
122 aqueous fluids over a wide range of pressures and temperatures, but they primarily focused on the  
123 CC  $\theta$ . Laporte and Provost (2000) theoretically investigated the  $\theta$  in the system with simplified  
124 surface energy anisotropy and reported that the relationship between the mean equilibrium  $\theta$  and  
125 the ratio of the grain boundary to the surface energy is close to the isotropic case. Nevertheless,  
126 empirical investigation of the facet-bearing dihedral angles concerning crystallographic  
127 orientations remains unresolved for actual mineral–fluid systems.

128 Investigating the grain boundary plane distribution (GBPD) can provide a mineralogical  
129 understanding of angle-types in terms of the FF, FC, and CC angles. Some researchers previously  
130 investigated GBPD in the fluid-free olivine polycrystals and found that low Miller Index planes  
131 preferentially appears in the grain boundaries (Faul & Fitz Gerald, 1999; Marquardt et al., 2015).  
132 If such specific grain boundary planes (GBPs) preferentially appear at the facet-bearing triple  
133 junctions in the mineral–fluid system, they may significantly control  $\theta$  of the facet-bearing angles

134 and its resultant fluid pore geometry. However, previous studies did not distinguish the grain  
135 boundary type in terms of the angle-types (i.e., FF, FC, and CC), and the GBPD has not been  
136 examined in the fluid-bearing system.

137 In this study, we investigated the facet-bearing (i.e., FF and FC)  $\theta$  in the run products of  
138 the olivine–fluid systems previously obtained by piston–cylinder experiments at various pressures  
139 (P: 1–3 GPa), temperatures (T: 800–1100 °C), and fluid compositions (pure H<sub>2</sub>O, H<sub>2</sub>O–NaCl, and  
140 H<sub>2</sub>O–CO<sub>2</sub> systems) (Huang et al., 2019, 2020). These results were compared with the CC  $\theta$  to  
141 clarify the effect of faceting. Moreover, we examined the crystallographic orientation of the olivine  
142 aggregate and identified the GBPD at triple junctions with different angle-types to evaluate the  
143 influence of the crystallographic orientations on  $\theta$ . Based on the results, we discussed the origin  
144 of faceting and its effect on  $\theta$  and inferred the consequences of faceting on the fluid connectivity,  
145 fluid distribution, and permeability anisotropy in the olivine–fluid system under static and sheared  
146 mantle conditions.

147 **2. Methods**

148 **2.1. Samples**

149 We analyzed the run products of the olivine–fluid systems previously obtained by Huang  
150 et al. (2020, 2019). To constrain the P–T and fluid composition dependency of the facet-bearing  
151  $\theta$ , we selected 19 samples that cover a wide range of experimental P–T conditions (1–3 GPa and  
152 800–1100 °C) and fluid compositions (H<sub>2</sub>O, H<sub>2</sub>O–CO<sub>2</sub> with  $X_{\text{CO}_2} = \text{CO}_2/(\text{H}_2\text{O}+\text{CO}_2) = 0.5$  in  
153 molar ratio), and H<sub>2</sub>O–NaCl with 5.0 and 27.5 wt.%NaCl). The run products containing magnesite  
154 and orthopyroxene due to olivine carbonation (Huang et al., 2020) were not included in the present  
155 study to avoid the effect of mineral species other than olivine.

156       Herein, we summarize the experimental procedures employed in a previous study (Huang  
157       et al., 2020, 2019) to synthesize the samples. High P–T experiments were conducted at Bayerisches  
158       Geoinstitut, University of Bayreuth, using end-loaded piston–cylinder apparatus. Piston diameters  
159       of 3/4 inch and 1/2 inches were used for the experiments at pressures of 1–2 GPa and 3 GPa,  
160       respectively, along with a standard Talc–Pyrex assembly (Keppler et al., 2003). The starting  
161       material was San Carlos olivine powder ( $\text{Fo}_{91}\text{Fa}_9$ ) with grain sizes of 38–53  $\mu\text{m}$ . Deionized and  
162       distilled water were used as the pure  $\text{H}_2\text{O}$  sources. Pure oxalic acid dihydrate ( $\text{C}_2\text{H}_2\text{O}_4 \cdot 2\text{H}_2\text{O}$ ) was  
163       used as the  $\text{CO}_2$  source. To obtain the  $\text{NaCl}$  solution, we dissolved reagent-grade  $\text{NaCl}$  (99.99%  
164        $\text{NaCl}$ ) in deionized and distilled water at room temperature ( $\sim 25^\circ\text{C}$ ) and atmospheric pressure.  
165       Water and hydrous oxalic acid were mixed to obtain the target  $X_{(\text{CO}_2)}$ . The olivine powder,  
166       combined with around 3.0 wt% fluid, was loaded into the end-welded noble metal capsule that was  
167       sealed by arc welding. The Au capsules (2.2 mm outer diameter) and  $\text{Au}_{80}\text{Pd}_{20}$  alloy capsules (2.0  
168       mm outer diameter) were used for experiments at 800–1000  $^\circ\text{C}$  and 1100  $^\circ\text{C}$ , respectively. The  
169       detailed procedures employed for the high P–T experiments were provided by Huang et al. (2019,  
170       2020). The run duration ranged from 72 h to 211 h, depending on the target temperature. The  
171       experimental conditions and results are summarized in Table 1. In our experiments,  $\text{CO}_2$  was  
172       assumed to be the predominant C species based on previous studies (Allen & C., 1972; Huang et  
173       al., 2020; Médard et al., 2008).

174       The post-run capsules were cut using a diamond wire saw to expose the run products. The  
175       run products were then impregnated with an epoxy resin under a vacuum. We first polished these  
176       products using the sandpaper and diamond past with particle sizes down to 1.0  $\mu\text{m}$  and then a 0.06  
177        $\mu\text{m}$  colloidal silica suspension. For electron backscattered diffraction (EBSD) analysis, the

178 samples were polished with colloidal silica suspension for more than 10 h using an automatic  
179 vibratory polishing machine (VibroMet, Buehler Ltd.).

180 **2.2. Scanning Electron Microscope (SEM)**

181 We observed polished cross-sections of the run charges using a field-emission type  
182 scanning electron microscope (FE-SEM; JSM-7100F, JEOL Ltd.) with an accelerating voltage of  
183 15 keV. The mineral phases and micro-texture of samples were observed. We took FF and FC type  
184 triple junctions for quantitative analysis. More than 300 backscattered electron (BSE) or secondary  
185 electron (SE) images of  $1280 \times 960$  pixels were obtained for each run product with high  
186 magnifications and resolution, depending on the pore size.

187 **2.3. Dihedral angle measurement**

188 The apparent FF and FC  $\theta$  were measured at the triple junctions on the SEM images using  
189 the Image-J software. We followed the method used for the CC angle measurements in Huang et  
190 al. (2019, 2020). The median of measured angles was regarded as true  $\theta$  (Jurewicz & Jurewicz,  
191 1986). Generally, the median of measured angles is close to the true  $\theta$  value to the greatest extent  
192 when a sufficient number of angles are measured by using high magnification and high-resolution  
193 SEM images. However, a deviation between the median and true angle could have occurred when  
194 the sample suffered from severe plucking during cutting and polishing, which locally reduced the  
195 randomness of the apparent angle distribution. Although Cmiral et al. (1998) demonstrated that  $\theta$   
196 values obtained with transmission electron microscopy (TEM) was smaller than those measured  
197 from low magnification SEM images, our FE-SEM images were taken at a high magnification (up  
198 to 150,000) and provided clear images comparable with those by TEM. In this study, more than  
199 100 angles were measured on the acquired SE images for each angle-type for each sample. The

200 statistical error of the median value was estimated to be less than  $1.5^\circ$ , as discussed by Huang et  
201 al. (2020). The details of  $\theta$  selection and measurement are given in Huang et al. (2019).

202 **2.4. Electron Backscattered Diffraction (EBSD)**

203 To identify the crystallographic orientation of the olivine aggregate and its consequences  
204 on  $\theta$ , we mapped 10 representative samples by using FE-SEM equipped with an electron  
205 backscatter diffraction (EBSD; HKL Channel5, Oxford Instruments plc.) at Tohoku University.  
206 Analyses were conducted at an accelerating voltage of 15.0 kV. Two types of EBSD data were  
207 collected for each sample. One was obtained with lower magnification ( $\times 200\text{--}500$ ) to investigate  
208 the crystallographic preferred orientation (CPO) of the entire sample, and the other with higher  
209 magnification ( $\times 5,000\text{--}15,000$ ) to identify the crystallographic orientation near the fluid pool. The  
210 EBSD data were then processed using the MTEX MATLAB toolbox. Grain boundaries were  
211 detected using a threshold misorientation angle of  $10^\circ$ . Grains smaller than two or three pixels  
212 were removed, depending on the step size (250 nm). The grain-size distribution and CPO were  
213 constructed from one point per data point.

214

215

216

217

218

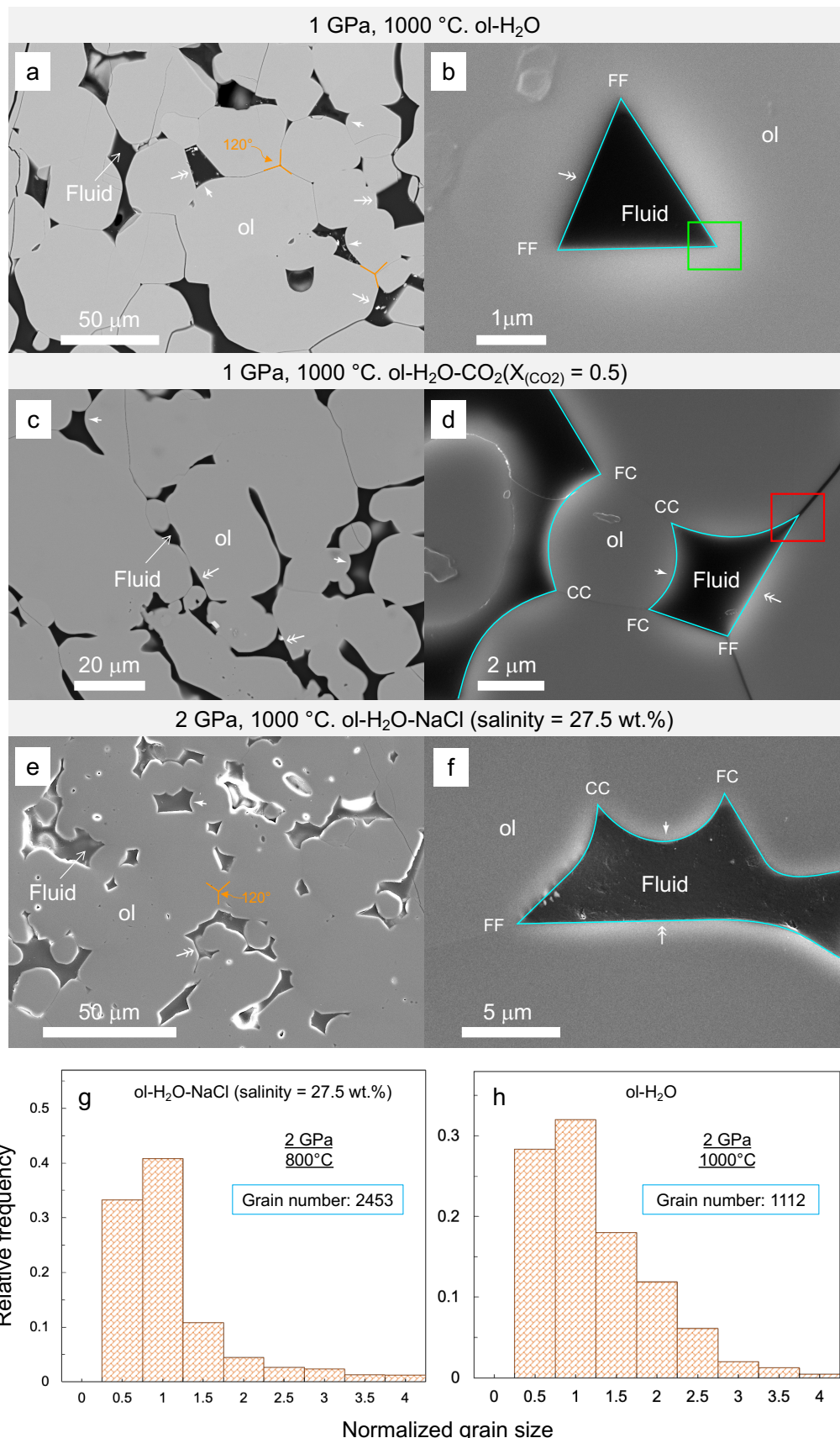
219

**Table 1. Experimental conditions and results**

Note: The fluid fraction in each experiment was ~3.0 wt.%. The true  $\theta$  value for each system was a median value  $\pm$

221 Note: The fluid fraction in each experiment was ~3.0 wt.%. The true  $\theta$  value for each system was a median value ±  
 222 1.5°. The analytical error for the faceting proportion was 0.5%. **a** the CC is cited from Huang et al. (2019); **b** the CC  
 223 is cited from Huang et al. (2020). The run products that were employed for the electron backscattered diffraction  
 224 (EBSD) and grain boundary plane distribution (GBPD) are marked in the table.  $X_{(CO_2)} = CO_2/(H_2O+CO_2)$  in mole.  
 225

226 Abbreviations: ol = olivine, FF = faceted-faceted angle, FC = faceted-curved angle, CC = curved-curved angle, All  
227 = all measured angles, I = angle-type independent group, D = angle-type dependent group.



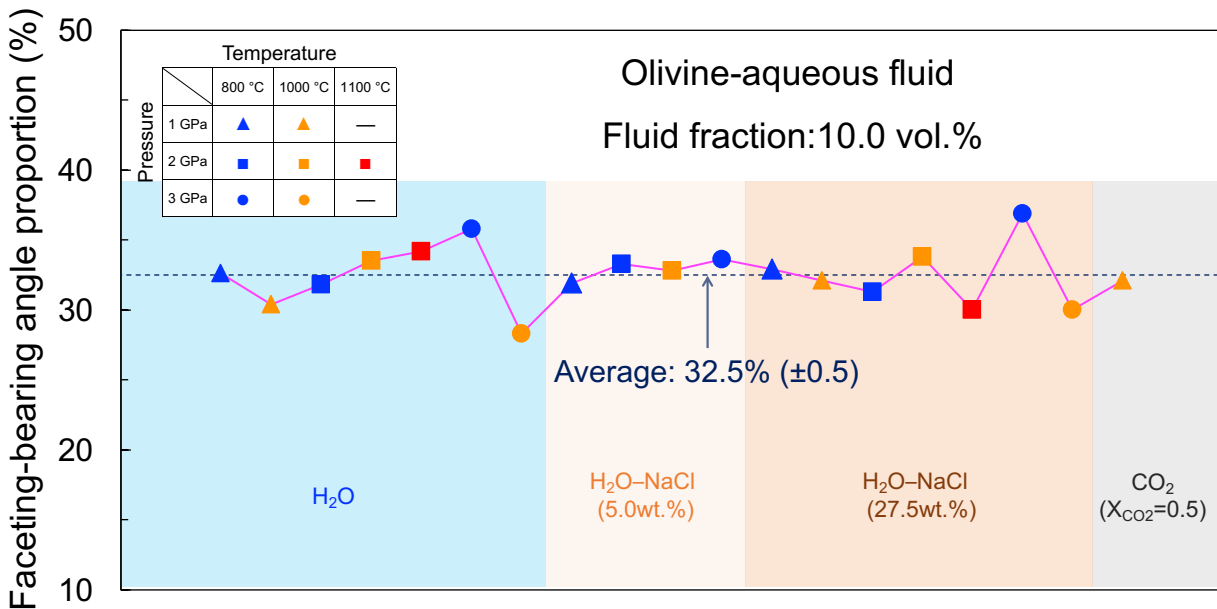
229 **Figure 1.** Representative SEM images and grain size distribution of the run products. **a** Backscattered electron  
230 image of the run product in the olivine–H<sub>2</sub>O system at 1000°C and 1 GPa for 120 h. **b** High-magnification secondary  
231 electron image of a typical triple junction in the olivine–H<sub>2</sub>O system at 1000°C and 1 GPa, which shows apparent FF  
232 angles. **c** Backscattered electron image of the run product in the H<sub>2</sub>O–CO<sub>2</sub> system ( $X_{\text{CO}_2} = 0.5$ ) at 1000°C and 1 GPa  
233 for 211 h. **d** High-magnification secondary electron image of the typical apparent θ in the H<sub>2</sub>O–CO<sub>2</sub> system ( $X_{\text{CO}_2} =$   
234 0.5) at 1000°C and 1 GPa for 211 h, which shows the coexistence of three types of apparent θ. **e** Backscattered electron  
235 image of the run product in the H<sub>2</sub>O–NaCl system (salinity = 27.5 wt.%) at 2 GPa and 1000°C for 120 h. **f** High-  
236 magnification secondary electron image of typical apparent θ in the H<sub>2</sub>O–NaCl system (salinity = 27.5 wt.%) at 2 GPa  
237 and 1000°C for 120 h. The run products are composed of mineral grains and epoxy resin-filled pores previously filled  
238 with aqueous fluid during the experiment. The orange marks denote the olivine–olivine–olivine triple junctions with  
239 intersection angles of ~120°, indicating the attainment of textural equilibrium. The white single and double arrows  
240 represent the curved and faceted interfaces, respectively. For the CC, FC, FF angles, the interfaces in **b**, **d**, and **f** are  
241 highlighted by cyan curves. The green and red rectangles illustrate suitable and unsuitable angles (i.e., with a crack)  
242 for measurement, respectively. **g**, Histogram of the grain size distribution in the H<sub>2</sub>O–NaCl system (salinity = 27.5  
243 wt.%) at 2 GPa and 800°C. **h**, Histogram of the grain size distribution in the H<sub>2</sub>O system at 2 GPa and 1000°C. The  
244 grain size distribution was normalized by the mean grain size of the recovered sample. The grain size is concentrated  
245 with a peak around the mean grain size. Abbreviations: ol = olivine, FF = faceted–faceted angle, FC = faceted–curved  
246 angle, CC= curved–curved angle.

247 **3. Results**

248 **3.1. Product phases and microstructures**

249 In all systems, the recovered samples are composed of olivine aggregates and intergranular  
250 fluid pores which are mostly filled with epoxy resin (Figure 1). The grain size of olivine in the run  
251 products increased with an enhancement of temperature, reaching ~110 µm at 1100°C through  
252 grain growth by Ostwald ripening and coalescence of two adjacent grains. The olivine grains were  
253 homogeneous in chemical compositions without obvious compositional zoning. Fluid-filled pores

were generally encompassed by three or more grains. Curved interfaces often coexisted with flat interfaces, even within a single pore (Figure 1). The curved interface results from the attainment of a constant mean curvature to minimize the surface energy by minimizing the surface area (Bargen & Waff, 1986; Waff & Faul, 1992), whereas the flat interface is attributed to the crystallographically controlled minimum interfacial energy (Yoshino et al., 2006). These two kinds of interfaces produce the three types of apparent  $\theta$ : CC, FC, and FF (Figure 1b, d, and f). The attainment of local interfacial energy minimization via balancing of interfacial tensions at triple junctions (i.e., textural equilibration) was demonstrated by 1) the occurrence of many olivine triple junctions with angles of  $\sim 120^\circ$  (Figure 1a, e) (e.g., Liu et al., 2018), 2) the cumulative frequency curves for apparent  $\theta$  that shows good agreement with the predicted curve for an equilibrated texture (Elliott et al., 1997), and 3) the concentrated normalized grain size distribution on the mean grain size (Figure 1g, h; Figure S3 of the Supporting Information) (Faul, 1997; Huang et al., 2021). This is supported by the fact that the experimental durations (72–211 h) were sufficiently long for attaining textural equilibrium compared with those in previous studies (e.g., 12 h for a grain size of 10  $\mu\text{m}$  at 727°C, Holness & Siklos, 2000). We measured the apparent FF and FC angles with clear interfaces (e.g., angles denoted by green rectangles in Figure 1b) and excluded those affected by cracks (e.g., the angle indicated by the red rectangle in Figure 1d).



271  
272 **Figure 2. The faceting-bearing angle proportion measured from the olivine–fluid system.** The results were  
273 calculated from 19 run products with a 10.0 vol.% fluid fraction. The average of 19 values is shown in the panel. The  
274 analytical error of each value is 0.5%. The P–T condition and fluid composition for each sample are shown in the  
275 panel.

276 **3.2. Proportion of faceting-bearing angles**

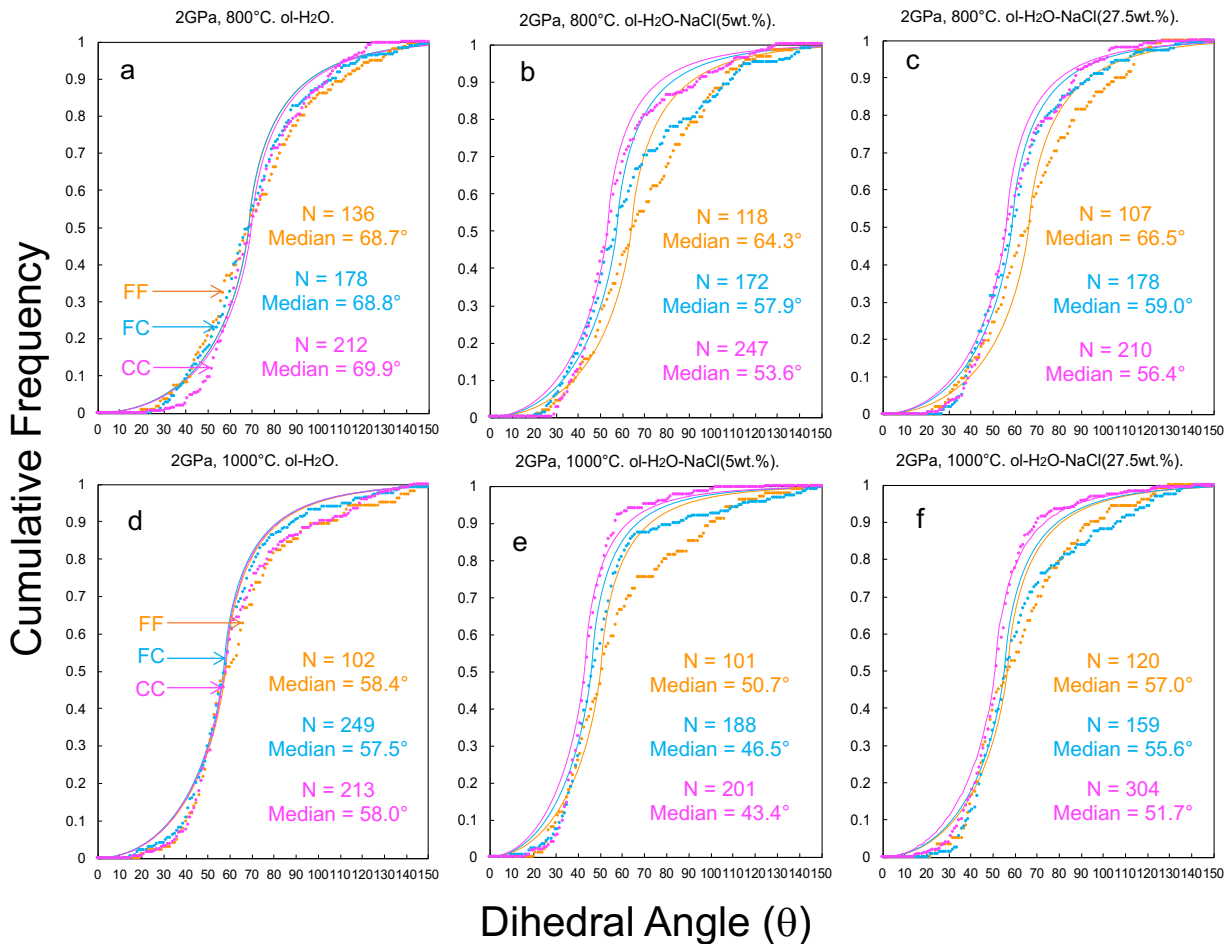
277 The proportion of facet-bearing angles (i.e., FF and FC angles) was evaluated from the  
278 SEM images of each recovered sample using Image–J (Figure 2). A total of 5025 angles were  
279 counted from the 19 samples (Table 1). To avoid the potential effect of heterogeneity in the angle–  
280 type distribution, we processed several images and obtained an average value for each sample.  
281 Although minor fluctuation occurs, the facet-bearing angle proportion is almost constant at  
282 approximately 32.5% ( $\pm 0.5$ ) without systematic P–T and fluid composition dependences. Namely,  
283 the FF and FC angles constituted approximately 1/3 of the dihedral angles. It is well demonstrated  
284 that the proportion of faceting is primarily controlled by  $\phi$  and that the faceting proportion  
285 increases with an increase in the liquid fraction in the solid–liquid system (Watson & Lupulescu,  
286 1993; Wark & Watson, 2000; Watson, 1999; Yoshino et al., 2005, 2006). Yoshino et al. (2005,

287 2006) reported that the faceting interface fraction in the olivine–basaltic melt system mostly fell  
288 in the range of 30.0–35.0 % with the melt fraction of 10.1–16.5 vol.%. Given an initial  $\phi$  of  
289 approximately 10.0 vol.% in our study, our calculated faceting proportion is roughly consistent  
290 with the previous research (Yoshino et al., 2006).

291 **3.3. Cumulative frequency of apparent dihedral angles**

292 The representative cumulative frequencies of the measured FF and FC angles in the  
293 olivine–fluid systems at 2 GPa are shown in Figure 3, in which the curves of the apparent CC  
294 angles from Huang et al. (2019, 2020) are plotted for comparison. The rest of the cumulative  
295 frequencies for the other conditions and histograms for all systems in this study are shown in  
296 Figures S4 and S5 of the Supporting Information. For all systems investigated, the cumulative  
297 frequencies mostly showed a sharp enhancement around the median  $\theta$ , and the frequency  
298 distribution histogram also showed a concentrated distribution of measured angles around the  
299 median value. In most cases, the CC angles sharply increase around the median angle, which is in  
300 accord with the theoretical prediction for the system with one true  $\theta$ . In contrast, the FF angles  
301 gradually increased around the median angle. This could indicate the expanded range of true  $\theta$   
302 owing to surface energy anisotropy on the facet-bearing angles (Laporte & Provost, 2000). In some  
303 cases (Figure 3), the data largely deviated from the theoretical curve in regions of high apparent  $\theta$ .  
304 This deviation was, first, attributed to the relatively small number of measured apparent FF angles.  
305 Second, this can be attributed to the presence of a very large  $\theta$  associated possibly with sub-grain  
306 boundaries, in which the misorientation between two adjacent grains is very small (Laporte et al.,  
307 1997). These two possible reasons cause the FF and FC angles to deviate more from the theoretical

308 curve than CC angle. Nevertheless, the median angles in such cases are assumed to represent the  
309 true value because the angles smaller than the median fit the theoretical line well.



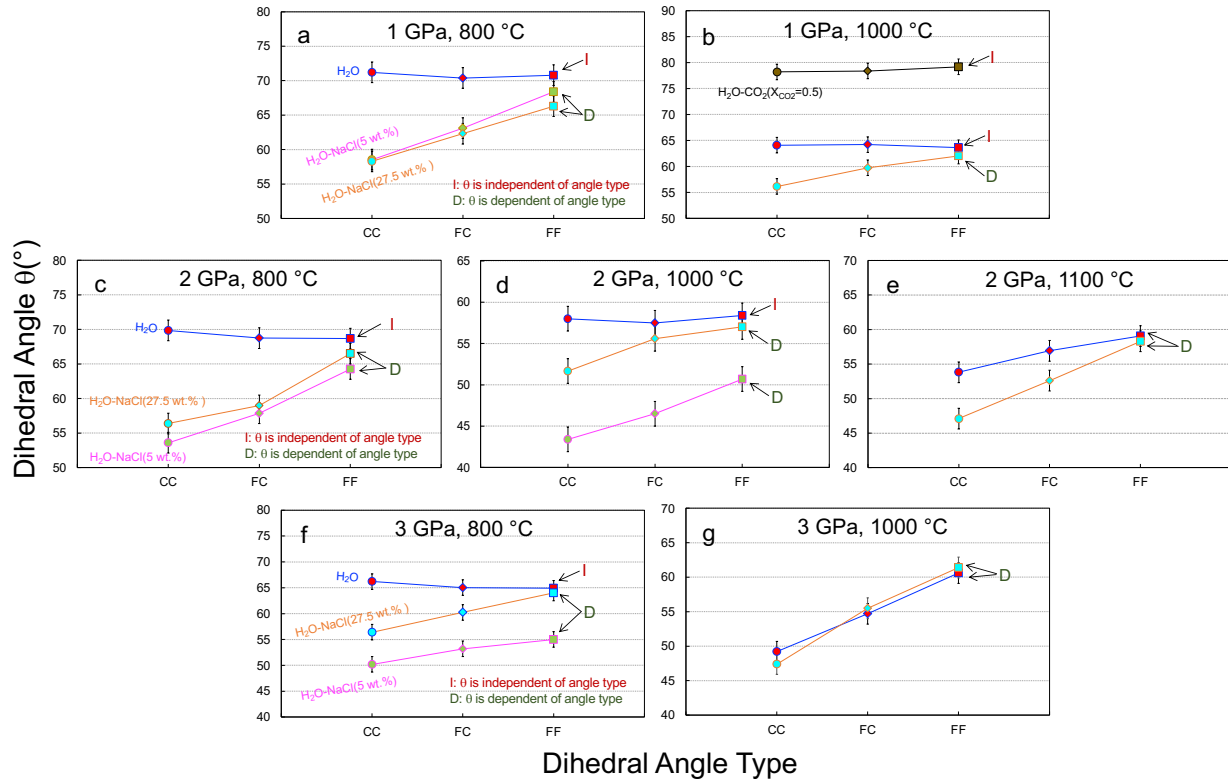
310

311 **Figure 3. Representative cumulative frequency curves of measured apparent dihedral angles ( $\theta$ ) in olivine–  
312 fluid systems at 2 GPa and 800–1000 °C.** The P–T condition and fluid composition are shown in the top of each  
313 panel. The facet-bearing angles (FC and FF) were measured in this study, while the data of the CC angles are from  
314 Huang et al. (2019, 2020). The median angle value and number (N) of the measured angles are shown for each case.  
315 The thin, solid curves represent the theoretical cumulative frequency curves obtained from the isotropic system with  
316 one true  $\theta$ . Abbreviations: FF = faceted–faceted angle, FC = faceted–curved angle, CC = curved–curved angle.

317

318     **3.4. Faceting effect on the median dihedral angle**

319         The angle-type dependence of the median  $\theta$  in the olivine–fluid systems at 1–3 GPa and  
320         800–1100 °C is shown in Figure 4. Two angle-type dependencies were recognized according to  
321         the fluid compositions and P–T conditions. The angle values were comparable among the CC, FC,  
322         and FF in the H<sub>2</sub>O systems at relatively low P–T conditions and the H<sub>2</sub>O–CO<sub>2</sub> system. In contrast,  
323         the median angle of the facet-bearing angles was higher than that of the CC angle in the H<sub>2</sub>O  
324         systems under higher P–T conditions and the H<sub>2</sub>O–NaCl systems. Hereafter, the former and latter  
325         systems are called as I group (angle-type independent group) and D group (angle-type dependent  
326         group), respectively. The corresponding groups for each run product are summarized in Table 1.  
327         Under each P–T condition, FC and CC angles showed a relatively wide variation in  $\theta$  between the  
328         H<sub>2</sub>O and H<sub>2</sub>O–NaCl systems, except for the results at 3 GPa and 1100°C, whereas FF angle was  
329         generally characterized by limited  $\theta$  variations. The  $\theta$  in the H<sub>2</sub>O–CO<sub>2</sub> system at 1GPa and 1000°C  
330         was larger than those of the other fluid compositions irrespective of the angle-type. In the H<sub>2</sub>O–  
331         NaCl (5.0 wt.% NaCl) systems, the  $\theta$  values of the FF angle are similar (Figure 4a and c) or smaller  
332         by 5–10° than those in the H<sub>2</sub>O and H<sub>2</sub>O–NaCl (27.5 wt.% NaCl) systems at the same P–T  
333         conditions (Figure 4d and f).



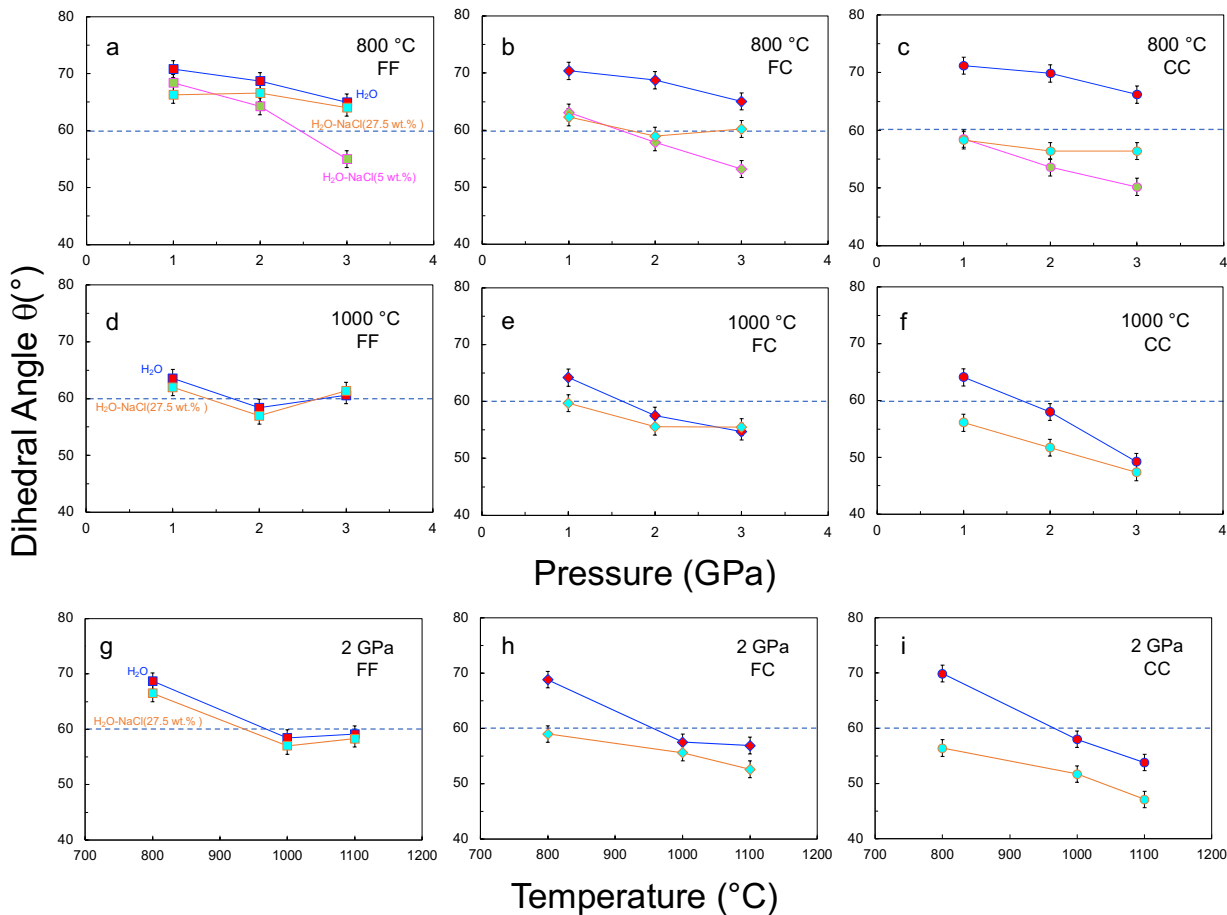
334

335 **Figure 4.** Faceting dependence of the median dihedral angles ( $\theta$ ) in the olivine–fluid system at 1–3 GPa and  
 336 800–1100 °C. Different colors in each panel denote the fluid compositions. The CC data are cited from Huang et al.  
 337 (2019, 2020). The error bar of  $\pm 1.5^\circ$  is shown in the panels. Abbreviations: FF = faceted–faceted angle, FC = faceted–  
 338 curved angle, CC = curved–curved angle, I = angle-type independent group, D = angle-type dependent group.

339 **3.5. P–T dependence of the median dihedral angles in the different fluid systems**

340 The P–T dependence of the median FF and FC angle in the olivine–fluid systems measured  
 341 in this study is shown in Figure 5, along with the CC angle reported by Huang et al. (2019). The  
 342 CC angle decreases with increasing pressure and temperature (Figure 5c, f, and i), corresponding  
 343 to the increase in olivine solubility under high P–T conditions (Huang et al., 2019). On the other  
 344 hand, the P–T dependence of the FC and FF angles was not obvious compared to that of the CC  
 345 angle. In particular, the FF angles showed a stepwise change in  $\theta$  but had similar  $\theta$  values (Figure  
 346 5a, d, and g). These findings suggest that factors other than solubility variation dominantly

347 controlled  $\theta$  of the FF angles. More discussion is given in Section 4.1 based on the EBSD results.  
 348 It is worth noting that the median values of the FF angle were larger than, or close to,  $60^\circ$  in most  
 349 cases.



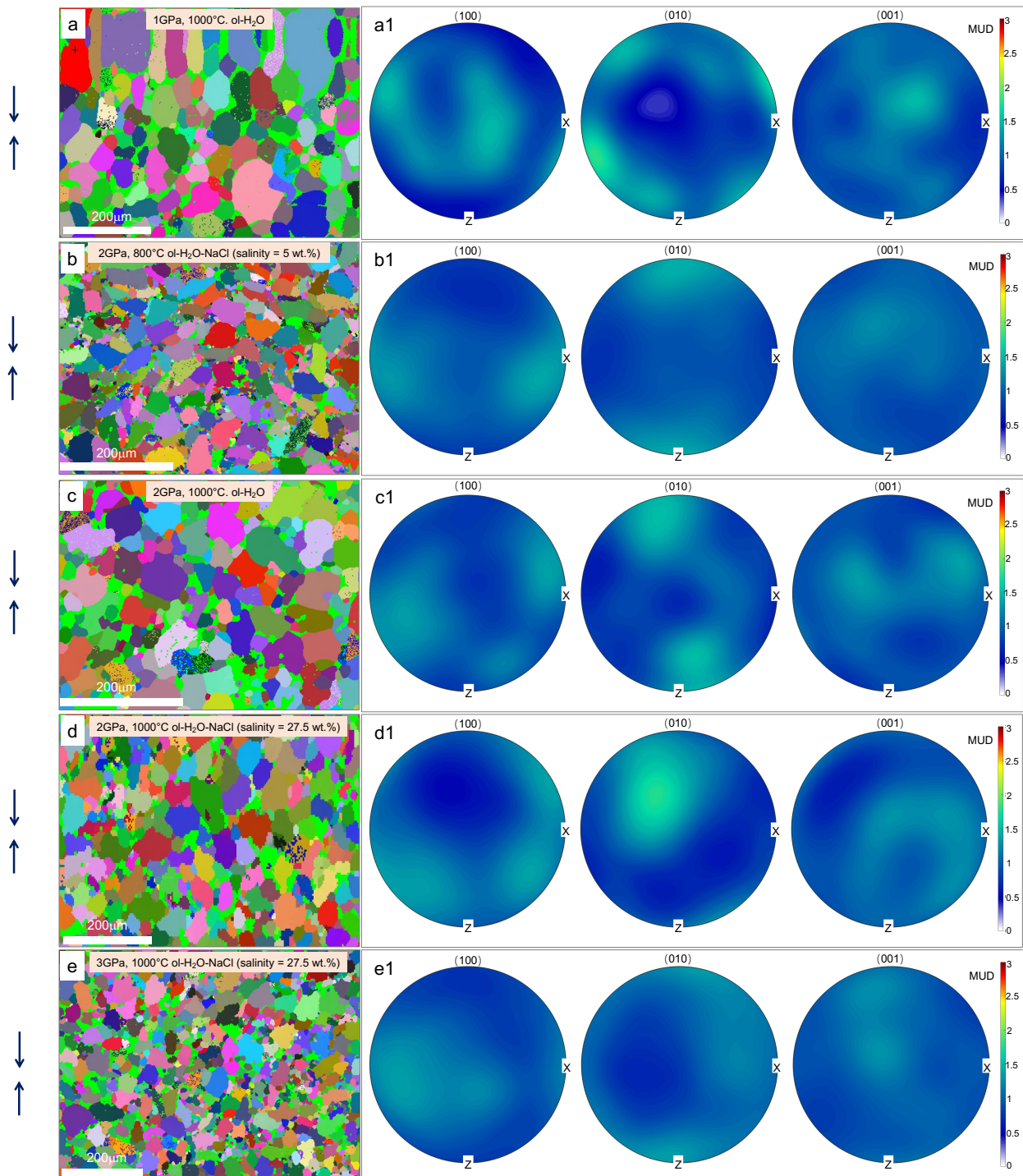
350  
 351 **Figure 5. Pressure and temperature dependence of the median dihedral angles ( $\theta$ ) in the olivine–fluid system.**  
 352 a-f Pressure dependence at 800–1000 °C. g-i. Temperature dependence at 2 GPa. The P-T condition and fluid  
 353 composition are shown in each panel. The CC data are from Huang et al. (2019). The error bar of  $\pm 1.5^\circ$  is shown along  
 354 with the median angle. The blue dash line represents  $\theta$  of  $60^\circ$ . Abbreviations: FF = faceted–faceted angle, FC =  
 355 faceted–curved angle, CC = curved–curved angle.

356  
 357

358     **3.6. Crystallographic orientation of olivine**

359         Figure 6 shows the representative EBSD maps and pole figures obtained from the five  
360 recovered samples. Figure S6 of the Supporting Information shows the rest of maps and pole  
361 figures. Our samples exhibited a merely weak (010) CPO (i.e., the *b* axis was slightly parallel to  
362 the compaction direction), regardless of the P–T conditions and fluid compositions. It was not as  
363 intense as the strong CPO that developed in the deformed olivine aggregate (Pommier et al., 2018).  
364 The weak CPO in this study is reasonable because the cell assembly of the piston–cylinder  
365 experiments with materials softened at high P–T conditions have been developed to avoid intense  
366 differential stress. Figure 7 shows the olivine grains' high-magnification orientation maps and the  
367 corresponding SE images. Additional figures related to the EBSD data processing are provided in  
368 Figures S7–S10 of the Supporting Information. If two adjacent grains have the same orientation,  
369 the apparent  $\theta$  between the two grains will be large because of the small grain boundary energy  
370 (white circles in Figure 7a1–d1). Further analyses on the crystallographic orientations of the GBPs  
371 are described in the discussion.

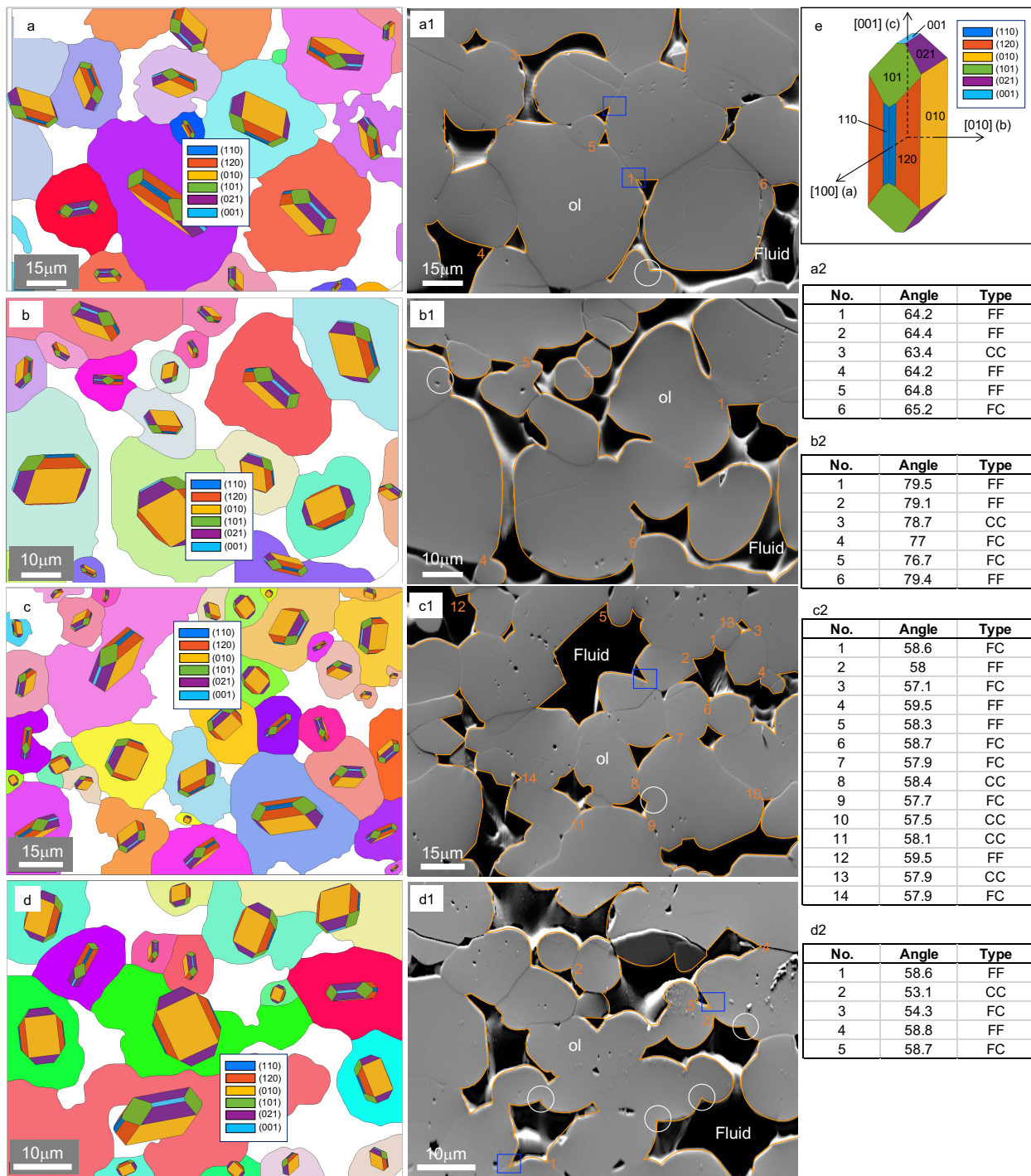
372



373

374 **Figure 6. Representative EBSD maps and corresponding pole figures.** a–e, EBSD maps of recovered olivine  
 375 aggregate in olivine–fluid systems. The small points within grains are attributed to the noise, crystal defects, and fluid  
 376 inclusions, which are mostly removed via denoise processes. In these systems, all grains are olivine with different  
 377 orientations. a1–e1, Pole figures to show the crystallographic orientations of (100), (010), and (001) corresponding to

378 a–e. The intensities in the color bar are multiples of the uniform distribution (MUD). The P–T condition and fluid  
 379 composition are shown at the top of a–e. The arrow on the left side represents the compaction direction (parallel to  
 380 the direction of piston movement).



381

382 **Figure 7. The olivine grains' representative 3-D crystal orientation and corresponding SE image in the olivine–**  
383 **fluid system.** EBSD mappings with 3-D crystal orientation of olivine in the H<sub>2</sub>O system at 1 GPa and 1000°C **(a)**, in  
384 the H<sub>2</sub>O–CO<sub>2</sub>(X<sub>(CO<sub>2</sub>)</sub>=0.5) system at 1 GPa and 1000°C **(b)**, in the H<sub>2</sub>O system at 2 GPa and 1000°C **(c)**, and in the  
385 H<sub>2</sub>O–NaCl (27.5wt%) system at 2 GPa and 1000°C **(d)**. Colored and white areas denote olivine grains and fluid pools,  
386 respectively. The 3-D crystal orientation was visualized for each grain in the high magnification images by showing  
387 the oriented olivine crystal with an idealized morphology. Even though the grain configurations in **a–d** are slightly  
388 altered during EBSD data processes such as denoising and binarization, those essentially have no effects on the  
389 orientation identification. **e**, Crystal habit of single olivine crystal. **a1–d1**, Secondary electron images of recovered  
390 olivine aggregates corresponding to **a–d**. Olivine grains have a grey color, and fluid pools are black areas that are  
391 sometimes filled by resin. An orange outline visually emphasizes the interface between the olivine and fluids, and the  
392 apparent angles with a sequenced number are examples of analyzed angles and corresponding grain boundaries. **a2–**  
393 **d2**, Dihedral angle–types, and their values in terms of FF, FC, CC corresponding to measured angles in **a1–d1**. These  
394 angles have values close to the corresponding median  $\theta$ . The white circle in **a1–d1** represents  $\theta$  of two grains that have  
395 the same orientation, leading to a larger  $\theta$  due to low misorientation of two adjacent grains. The blue square in **a1**, **c1**,  
396 and **d1** represents  $\theta$  that has one shared flat plane for both grain boundary and interfacial boundary. Abbreviations: ol  
397 = olivine, FF = faceted–faceted angle, FC = faceted–curved angle, CC = curved–curved angle.

398 **3.7. Grain boundary plane distribution**

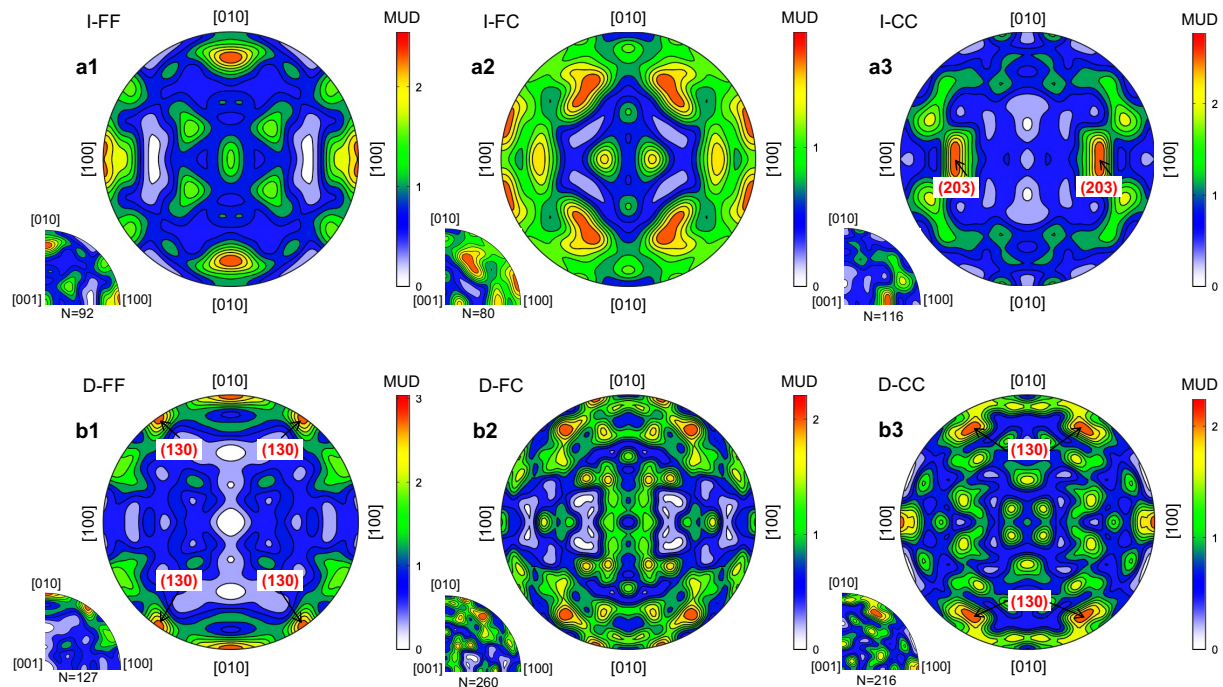
399 To clarify the crystallographic orientation of olivine on GBPs, we evaluated the GBPD for  
400 the grain boundaries at the FF, FC, and CC angles on a high magnification orientation map (Figure  
401 7). In general, GBPs are not vertical; they tend to incline at various degrees with respect to the  
402 polished cross-section of the sample. In the two-dimensional (2-D) SEM images, we cannot  
403 recognize how much these planes inclined. To mitigate this problem, we focused on the olivine–  
404 fluid–olivine triple junction with apparent dihedral angles lower than the median value + 5° and  
405 assumed that their grain boundaries were subvertical to the polished section. For example, in the  
406 system with one true  $\theta$  of 60°, 71% of the apparent dihedral angles fell within the range from 0 to

65°, in which 68% of GBPs formed an angle greater than or equal to 67° with respect to the sectioning plane. Thus, we inferred the representative errors of ~23° in our GBPD analyses. More details about the errors of the GBPD analyses are provided in the Supporting Information Note 1 and Figures S1–S2. At such triple junctions, we determined the crystallographic orientations of olivine sharing the assumed vertical GBPs in the nine samples, including both I and D groups. In the calculation, we used the Euler angles derived from the EBSD analysis and the trend of the GBPs with respect to the horizontal side of the corresponding SEM image. The equivalent olivine orientations obtained for each angle-type were stereologically projected in the crystal reference frame, as shown in Figure 8.

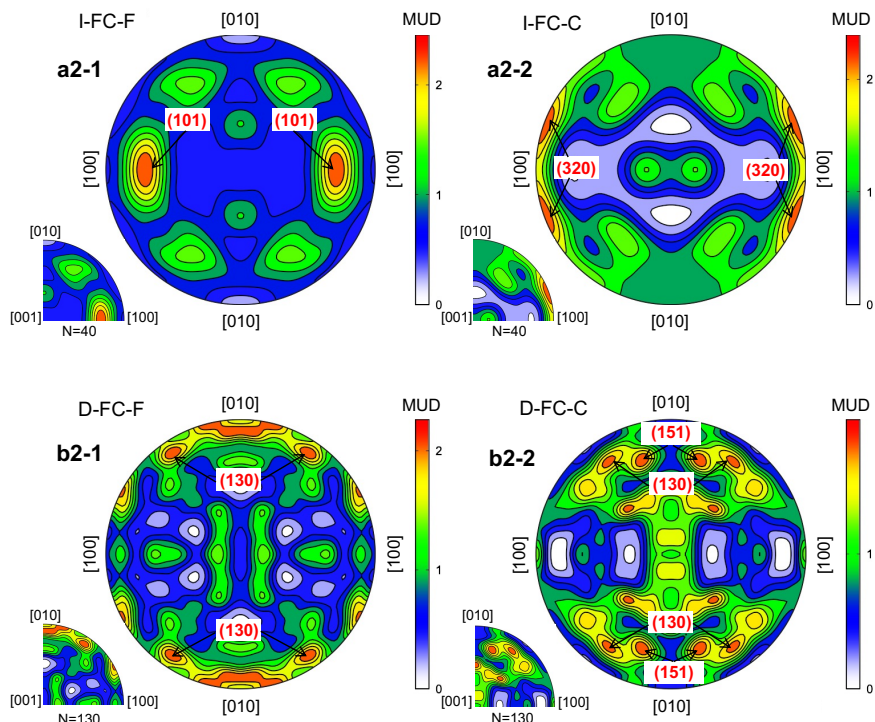
In the I group, the low Miller Index planes such as (100) and (010) were dominant at the grain boundaries of the FF triple junctions, whereas the GBPs of the CC triple junctions were often characterized by a higher Miller Index such as (203). Note that the multiples of uniform density (MUD) spots indexed as (101) and (100) in Figure 8a1 are indistinguishable because of the tilt of the GBP. In the D group, the GBPs of the FF triple junctions were focused on (010), but equally around (130), which was interpreted as a broad concentration around (010). Although the differences in these planes were out of the possible errors of  $\pm \sim 20^\circ$  in our analyses, the large variations in the true  $\theta$  at the FF angle especially in the D groups (Figure 3b, c, e, f, Section 3.3) could cause the apparent broadening of the concentration around (010) beyond the assumed errors. At the CC triple junctions, the high Miller Index planes around (130) is dominant, and the (100) is relatively weak. The GBPD at the FC triple junctions tended to exhibit mixed characteristics of the FF and CC results in both groups. Although the amount of the data was reduced, the GBPs at the faceted and curved sides were separately analyzed at the FC triple junctions, as shown in Figure 9. As in the FF and CC junctions, the GBPs at the faceted side were dominated by low Miller Index

430 planes such as (101) and (010), whereas the GBPs at the curved side rather preferred the high  
 431 Miller Index planes such as (320) and (151). This indicates that the GBPDs observed in the FF and  
 432 CC triple junctions are likely true. The weak CPO developed in the run products did not  
 433 significantly affect the results.

434 Marquardt et al. (2015) found that the fluid-free olivine aggregates have a preferred (100)  
 435 plane of the grain boundary, which is different from the preferential appearance of the (100),  
 436 (010), and (101) planes on the grain boundaries at the FF angle in present study. This discrepancy  
 437 is most likely due to the high  $\phi$  in our study. The crystal habit of olivine grown freely in the fluid-  
 438 rich system is characterized by the dominant (010) plane (Waff & Faul, 1992). Previous studies  
 439 have shown that the (010) plane of olivine has the lowest energy, followed by the (100) and (001)  
 440 planes in fluid/melt systems (Deer et al., 2013; Gurmani et al., 2011; de Leeuw et al., 2000; Watson  
 441 et al., 1997), indicating a low grain boundary energy in the FF triple junctions.



443 **Figure 8. Pole figure of grain boundary plane distribution.** **a1–a3**, Grain boundary plane distribution in the **I** group  
 444 (i.e., the systems where the  $\theta$  values are independent of the angle-type). **b1–b3**, Grain boundary plane distribution in  
 445 the **D** group (i.e., the systems where the faceting increases  $\theta$ ). The equivalent olivine orientations obtained in the  
 446 analysis were rearranged into the first quadrant to make the results more evident. Subsequently, by assuming that the  
 447 grain boundary planes were equally distributed in each quadrant, the orientations in the first quadrant were copied in  
 448 the other quadrants to obtain the pole figure. The analyzed number (N) in the first quadrant is shown at the lower left  
 449 in each pole figure. MUD is the multiples of uniform density, shown by the color bar's intensities. The Miller Indexes  
 450 were marked around the high MUD. Abbreviations: FF = faceted–faceted angle, FC = faceted–curved angle, CC =  
 451 curved–curved angle, I = angle–type independent group, D = angle–type dependent group.



452  
 453 **Figure 9. Pole figure of FC angles.** Pole figure of grain boundary plane distributions (GBPDs) of faceted (**a2–1** and  
 454 **b2–1**) and curved (**a2–2** and **b2–2**) sides at the FC triple junction for **I** group (i.e., the systems where the  $\theta$  values are  
 455 independent of the angle-type; **a2–1** and **a2–2**) and **D** group (i.e., the systems where the faceting increases  $\theta$ ; **b2–1**  
 456 and **b2–2**). The data were plotted in the same way as in Figure 8. The analyzed number (N) in the first quadrant is  
 457 shown at the lower left in each pole figure. MUD represents the multiples of uniform density, which shows the

458 intensities in the color bar. The Miller Indexes were marked around the high MUD. Abbreviations: FC = faceted–  
459 curved angle, F = grain boundary at the faceting side, C = grain boundary at the curved side, I = angle-type  
460 independent group, D = angle-type dependent group.

461 **4. Discussion**

462 In section 4.1, we calculated the theoretical FF angle based on the ideal crystal habit and  
463 discussed the primary factor controlling  $\theta$  of FF angle. Based on our results, we further discuss the  
464 effect of the faceted interface on the fluid distribution under static conditions in Section 4.2 and  
465 the permeability anisotropy in the sheared mantle in Section 4.3.

466 **4.1 Primary factor controlling  $\theta$  of FF angle**

467 Under high P–T conditions, enhanced olivine solubility significantly decreased the  
468 interfacial energy with the fluid, resulting in an obvious P–T dependence of  $\theta$  of the CC angle  
469 (Huang et al., 2019, 2020). However,  $\theta$  of the FF angle was less sensitive to P–T conditions than  
470 that of the CC angle, with discrete values. The variation cannot explain such characteristics in  
471 interfacial energy under P–T conditions. Laporte and Provost (2000) theoretically investigated an  
472 anisotropic system and showed that  $\theta$  of the FF angle was controlled by the crystallographic  
473 orientation of two adjacent minerals. In this study, our GBPD analyses revealed that low Miller  
474 Index planes, such as (100), (010), and (101), preferentially appeared at the GBPs of the FF angle  
475 (Figures 8 and 9). Because the faceted mineral–fluid interfaces appeared to have low Miller indices,  
476 the  $\theta$  value of the FF angle can be estimated from the angles between the GBPs of (100), (010),  
477 (101), and the other low Miller Index olivine surfaces. To test this inference, we calculated the  
478 angles between the GBPs of (100), (010), and (101) and the low-energy faceted planes of (001),  
479 (011), (110), (101), (120), and (021) based on the crystal planes appearing in the ideal habit of

480 olivine crystals (Figure. 7e). The calculations were made for asymmetrical configurations and  
481 symmetrical ones, because the olivine aggregate sintered in the present study showed a weak CPO  
482 (i.e., the random alignment of grains). Triple junctions that one extended grain boundary plane  
483 acts as one of interfaces, were considered as an extreme case (Flat face in Table 2). All the  
484 calculated configurations are presented in Table 1 of the Supporting Information and the angles  
485 consistent with the experimentally obtained FF  $\theta$  (i.e., 50–55°, 55–65°, 65–70°, and 75–80°) are  
486 summarized in Table 2. The calculated candidates cover these experimental values in Table 2. For  
487 instance, the measured I-Type FF  $\theta$  in the H<sub>2</sub>O–CO<sub>2</sub> system at 1 GPa and 1000°C, is 79.2°. This  
488 may correspond to the calculated dihedral angles of 77.0° and 81.4° from a symmetrical triple  
489 junction composed of (100)–(101) and (010)–(021) planes, respectively, or 81.5°, 79.2°, and 80.1°  
490 from an asymmetrical triple junction composed of the (100)–(101) and (100)–(120), (010)–(021)  
491 and (100)–(101), and (101)–(120) and (100)–(110), respectively. In fact, the GBPs can be slightly  
492 inclined from the assumed planes, which may have resulted in a relatively broad distribution of  
493 the apparent FF  $\theta$  as shown in Figure 4. For a symmetrical triple angle configuration, the two  
494 grains come in contact with the same low Miller index planes and share the lattice, whereas the  
495 lattice may not be highly shared for an asymmetrical triple angle configuration. The discrepancy  
496 in the grain boundary energy for these two cases is most likely negligible because the low Miller  
497 index GBPs have intrinsically low-surface energy (e.g., Yoshino et al., 2006). Thus, the  $\theta$  value of  
498 the FC angle may be controlled by both interfacial energy and crystallographic orientation,  
499 resulting in the FC angle showing intermediate characteristics between the FF and CC angles.

500  
501  
502  
503  
504

505

**Table 2. Theoretical FF angle between two crystal planes**

<b>Crystal</b>	<b>GBCP</b>	<b>IBCP</b>	<b>ACP(°)</b>	<b>Calculated FF Angle(°)</b>	<b>Configuration</b>	<b>Measured FF angle(°)</b>
C1	100	110	25.0	50.0	Symmetrical	
C2	100	110	25.0			
C1	101	001	51.5	51.5	Flat face	50–55
C1	101	120	55.1	55.1	Flat face	
C1	100	110	25.0	63.5	Asymmetrical	55–65
C2	100	101	38.5			
C1	100	110	25.0	65.7	Asymmetrical	
C2	100	021	40.7			
C1	101	021	66.2	66.2	Flat face	
C1	100	110	25.0	68.0	Asymmetrical	65–70
C2	010	120	43.0			
C1	100	110	25.0	69.8	Asymmetrical	
C2	101	110	44.8			
C1	100	110	25.0	76.5	Asymmetrical	
C2	101	110	51.5			
C1	100	101	38.5	77.0	Symmetrical	
C2	100	101	38.5			
C1	100	101	38.5	79.2	Asymmetrical	
C2	010	021	40.7			
C1	100	110	25.0	80.1	Asymmetrical	75–80
C2	101	120	55.1			
C1	101	021	40.7	81.4	Symmetrical	
C2	101	021	40.7			
C1	100	101	38.5	81.5	Asymmetrical	
C2	100	120	43.0			

506

507

508

509

510

511

512

513

514

Note: The calculated FF angle was obtained by summing the two angles between two crystal planes (ACP). This configuration shows the geometry of the calculated dihedral angle. We assume that the two crystals (crystal 1, C1; crystal 2, C2) come in contact with same (symmetrical configuration) or different (asymmetrical configuration) low-Miller index planes to form the FF angle. Additionally, we show extreme cases where one flat plane is shared for both grain boundary and interfacial boundary. GBCP, grain boundary crystal plane; IBCP, interfacial boundary crystal plane. The crystal cell parameters ( $a=4.7540 \text{ \AA}$ ,  $b=10.1971 \text{ \AA}$ , and  $c=5.9806 \text{ \AA}$ ) employed for the angle calculation were obtained from Deer et al. (2013).

515

516    **4.2. Consequences of faceting on the fluid connectivity in the undeformed olivine–fluid**  
517    **system**

518       Our study demonstrated that ~1/3 of the dihedral angles in the olivine–fluid system are  
519    facet-bearing, irrespective of P–T conditions and fluid compositions (Table 1). The fluid pores  
520    surrounded by faceted interfaces are difficult to connect each other even at  $\theta < 60^\circ$ , which requires  
521    a threshold  $\phi$  for the establishment of a fluid network, as in the case of a CC angle  $> 60^\circ$  (Price et  
522    al., 2006). Thus, a system that includes both curved and faceted interfaces with low  $\phi$ , the bulk  
523    permeability may be reduced. Huang et al. (2021) measured the electrical conductivity of the fluid-  
524    bearing forsterite aggregate with various  $\phi$  under the textural equilibrium states at 1 GPa and 800°C  
525    in the H<sub>2</sub>O–NaCl system with 5.0 wt.% NaCl. The electrical conductivity measurements and the  
526    synchrotron X-ray computed CT imaging of the post run products showed that fluid pores were  
527    not interconnected at  $\phi$  of 0.51 vol.%. In contrast, they started to form the fluid network at  $\phi$  above  
528    2.14 vol.%. Although the CC angle can be lower than 60° under this experimental P–T condition  
529    (Huang et al., 2019), fluid interconnection was not established at  $\phi$  below ~1.0–2.0 vol.%. This  
530    could most likely be attributed to a presence of substantial number of faceted interfaces that  
531    increases  $\phi_c$  and decreases the permeability, as pointed out by Price et al. (2006).

532       Toramaru and Fujii (1986) examined the melt connectivity in peridotites composed of  
533    olivine, clinopyroxene, and orthopyroxene based on a bond percolation model with the melt  
534    stability at the grain edges and corners, namely, dihedral angles. They found that the partial melt  
535    was not stable at pyroxene-dominated grain edges and that the interconnection was established  
536    when pyroxene modal composition was lower than ~25–20 vol.% when the grain size of olivine  
537    and pyroxenes are similar. If we assume that the faceting triple junctions hampers the fluid

538 interconnection, an analogous discussion will be possible for the fluid connectivity in facet-bearing  
539 olivine aggregates. Given the slightly higher proportion of faceting triple junctions (28–36%;  
540 Table 1) than the above pyroxene modal composition of Toramaru and Fujii (1986), the electrical  
541 conductivity results of Huang et al. (2021), in which the fluid percolation was prohibited at  $\phi=0.51$   
542 vol.% but established at a small critical fraction (2.14 vol.%) seems consistent with the model  
543 prediction.

544 **4.3. Preferential appearance of faceted fluid pores in the sheared mantle**

545 Our study demonstrated that faceted olivine–fluid interfaces are preferentially  
546 accompanied by low Miller index GBPs such as (100), (010), and (101). The extensive occurrence  
547 of faceted crystallographic faces in deep-seated rocks can change the bulk permeability, elastic,  
548 anelastic, and electrical properties (Waff & Faul, 1992). Waff and Faul (1992) investigated the  
549 melt distribution in the texturally equilibrated olivine–melt system and found that the presence of  
550 the melt film along the pervasive faceted crystal interface was making  $\theta$  much smaller, and  
551 increasing the permeability of the bulk rock. However, the effect of the faceted interface on pore  
552 morphology and permeability obtained from olivine–fluid systems in the present study is different  
553 from that of olivine–melt system. Our results showed that the grain boundaries associated to the  
554 flat interface are dry and the FF and FC  $\theta$  were comparable to or larger than the CC angles, working  
555 against the establishment of fluid connectivity. This effect could be magnified under the shear  
556 stress such as the corner flow in subduction zones. In the deformed olivine aggregate with strong  
557 CPO, the crystal axes (i.e.,  $a$ ,  $b$ , and  $c$  axes) of olivine grains are aligned in specific directions  
558 depending on the temperature, olivine water content, and stress state (Jung et al., 2006; Jung &  
559 Karato, 2001; Karato et al., 2008; Kneller et al., 2005, 2008). This alignment may lead to low

560 Miller index planes dominating grain boundaries, thereby increasing the proportion of facet-  
561 bearing angles in the sheared mantle.

562 Jung and Karato (2001) examined the water-saturated olivine fabric under shear strain and  
563 found that the c axis was subparallel to the shear direction, and the b axis was perpendicular to the  
564 shear direction (B-type fabric). Therefore, in water-rich subduction zone, a B-type fabric is  
565 expected, in which the c axis is subparallel to the subduction direction and the b axis is  
566 perpendicular to the plate interface. Liu and Zhao (2017) detected the Vp anisotropy in the mantle  
567 wedge beneath Japan, supporting the hypothesis that the B-type fabric is dominant in the fore-arc  
568 mantle wedge. This type of grain alignment could produce abundant grain boundaries composed  
569 of the (100) and (010) planes parallel to the subduction direction to form many FF angles  
570 comparable to or larger than the CC angle, decreasing the permeability and electrical conductivity  
571 along the subduction direction. That is to say, the presence of faceting may contribute to the  
572 anisotropy of permeability and conductivity, which is important for understanding fluid flow, flux  
573 melting, anomalies of the electrical conductivity, and seismic wave velocities in subduction  
574 systems.

575 **5. Conclusion**

576 In this study, we determined quantitatively the effect of faceting on the olivine–fluid θ in  
577 different fluid systems ( $\text{H}_2\text{O}$ ,  $\text{H}_2\text{O}-\text{CO}_2$  ( $X_{\text{CO}_2}=0.5$ ),  $\text{H}_2\text{O}-\text{NaCl}$  (5.0 and 27.5 wt.% NaCl)) at 1–  
578 3 GPa and 800–1100 °C. The results show that 1/3 of olivine–fluid θ are faceted plane-bearing  
579 angles irrelative to the P–T conditions and fluid compositions. The θ measurement shows that in  
580 the  $\text{H}_2\text{O}$  systems at relatively low P–T conditions and in the  $\text{H}_2\text{O}-\text{CO}_2$  system, the facet-bearing  
581 angle values (i.e., FF, FC) are comparable to those of the CC angle. However, in the  $\text{H}_2\text{O}$  systems

582 at high P–T conditions and in the H<sub>2</sub>O–NaCl systems, the facet-bearing angle values (i.e., FF, FC)  
583 are larger than those of the CC angle. EBSD analyses show that the run products do not have an  
584 intense crystallographic preferred orientation (CPO) corresponding to static compression  
585 conditions. Strikingly, the grain boundary plane distribution (GBPD) revealed that the faceted and  
586 curved interfaces at facet-bearing triple junctions have grain boundary planes (GBPs) subjected to  
587 the low (e.g., (100), (010), (101)) and high (e.g., (130), (203), (320)) Miller Index faces,  
588 respectively. The calculation of  $\theta$  values between two adjacent crystal planes highly reproduces  
589 the measured values of the FF angles, which further supports the results of our GBPD analyses.  
590 Therefore, our results suggest the importance of crystallographic orientation in determine the  
591 origin of the FF angle. The presence of the FF angle and associated changes in fluid pore  
592 morphology will require a high fluid fraction for establishing the fluid networks. It will further  
593 lead to the permeability anisotropy and changes in geophysical characteristics, particularly for the  
594 mantle wedge settings where olivine CPO is expected.

## 595 **Acknowledgments**

596 This work was supported by JSPS KAKENHI Grant Nos. JP16H06348 and JP16K13903  
597 awarded to M. Nakamura, JSPS Japanese–German Graduate Externship, International Joint  
598 Graduate Program in Earth and Environmental Sciences, Tohoku University (GP–EES), and by  
599 the Ministry of Education, Culture, Sports, Science and Technology (MEXT) of Japan under its  
600 Earthquake and Volcano Hazards Observation and Research Program, the Core Research Cluster  
601 of Disaster Science in Tohoku University (Designated National University), and by the  
602 Tuguangchi Award for Excellent Young Scholar (E1510316) in Guangzhou Institute of  
603 Geochemistry, Chinese Academy of Sciences. We provide the datasets on figshare  
604 (<https://doi.org/10.6084/m9.figshare.19786252.v1>), including dataset of pole figure derived from  
605 EBSD data and dataset of FF angle calculation, to support our research.

607 **Reference**

- 608 Allen, C., J. (1972). The role of water in the mantle of the earth: the stability of amphiboles and  
609 micas. *24th International Geological Congress, Montreal*, 2, 231–240.
- 610 Angiboust, S., Pettke, T., de Hoog, J. C. M., Caron, B., & Oncken, O. (2014). Channelized Fluid  
611 Flow and Eclogite-facies Metasomatism along the Subduction Shear Zone. *Journal of*  
612 *Petrology*, 55(5), 883–916. <https://doi.org/10.1093/PETROLOGY/EGU010>
- 613 Cmíral, M., Fitz Gerald, J. D., Faul, U. H., & Green, D. H. (1998). A close look at dihedral angles  
614 and melt geometry in olivine–basalt aggregates: A TEM study. *Contributions to Mineralogy*  
615 and Petrology, 130(3–4), 336–345. <https://doi.org/10.1007/s004100050369>
- 616 de Leeuw, N. H., Parker, S. C., Catlow, C. R. A., & Price, G. D. (2000). Modelling the effect of  
617 water on the surface structure and stability of forsterite. *Physics and Chemistry of Minerals*,  
618 27, 332–341. <https://doi.org/10.1007/S002690050262>
- 619 Deer et al. (2013). An Introduction to the Rock-Forming Minerals (third edition). *The Canadian*  
620 *Mineralogist*, 51. <https://doi.org/10.3749/CANMIN.51.4.663>
- 621 Elliott, M. T., Cheadle, M. J., & Jerram, D. A. (1997). On the identification of textural equilibrium  
622 in rocks using dihedral angle measurements. *Geology*, 25(4), 355–358.  
623 <https://doi.org/10.1130/0091-7613>
- 624 Faul, U. H. (1997). Permeability of partially molten upper mantle rocks from experiments and  
625 percolation theory. *Journal of Geophysical Research: Solid Earth*, 102(B5), 10299–10311.  
626 <https://doi.org/10.1029/96jb03460>
- 627 Faul, U. H., & Fitz Gerald, J. D. (1999). Grain misorientations in partially molten olivine  
628 aggregates: an electron backscatter diffraction study. *Physics and Chemistry of Minerals*,  
629 26(3), 187–197. <https://doi.org/10.1007/S002690050176>
- 630 Gurmani, S. F., Jahn, S., Brasse, H., & Schilling, F. R. (2011). Atomic scale view on partially  
631 molten rocks: Molecular dynamics simulations of melt-wetted olivine grain boundaries.  
632 *Journal of Geophysical Research: Solid Earth*, 116(B12), 12209.  
633 <https://doi.org/10.1029/2011JB008519>
- 634 Hermann, J., Spandler, C., Hack, A., & Korsakov, A. v. (2006). Aqueous fluids and hydrous melts  
635 in high-pressure and ultra-high pressure rocks: Implications for element transfer in  
636 subduction zones. *Lithos*, 92(3–4), 399–417. <https://doi.org/10.1016/j.lithos.2006.03.055>
- 637 Holness, M. B., & Siklos, S. T. C. (2000). The rates and extent of textural equilibration in high-  
638 temperature fluid-bearing systems. *Chemical Geology*, 162, 137–153.  
639 [https://doi.org/10.1016/S0009-2541\(99\)00124-2](https://doi.org/10.1016/S0009-2541(99)00124-2)
- 640 Holness, M. B. (1992). Equilibrium dihedral angles in the system quartz–CO<sub>2</sub>–H<sub>2</sub>O–NaCl at  
641 800°C and 1–15 kbar: the effects of pressure and fluid composition on the permeability of  
642 quartzites. *Earth and Planetary Science Letters*, 114(1), 171–184.  
643 [https://doi.org/10.1016/0012-821X\(92\)90159-S](https://doi.org/10.1016/0012-821X(92)90159-S)

- 644 Holness, M. B. (1993). Temperature and pressure dependence of quartz–aqueous fluid dihedral  
645 angles: the control of adsorbed H<sub>2</sub>O on the permeability of quartzites. *Earth and Planetary*  
646 *Science Letters*, 117(3–4), 363–377. [https://doi.org/10.1016/0012-821X\(93\)90090-V](https://doi.org/10.1016/0012-821X(93)90090-V)
- 647 Huang, Y., Nakatani, T., Nakamura, M., & McCammon, C. (2019). Saline aqueous fluid  
648 circulation in mantle wedge inferred from olivine wetting properties. *Nature Communications*,  
649 10(1), 5557. <https://doi.org/10.1038/s41467-019-13513-7>
- 650 Huang, Y., Nakatani, T., Nakamura, M., & McCammon, C. (2020). Experimental constraint on  
651 grain–scale fluid connectivity in subduction zones. *Earth and Planetary Science Letters*, 552,  
652 116610. <https://doi.org/10.1016/j.epsl.2020.116610>
- 653 Huang, Y., Guo, H., Nakatani, T., Uesugi, K., Nakamura, M., & Keppler, H. (2021). Electrical  
654 Conductivity in Texturally Equilibrated Fluid–Bearing Forsterite Aggregates at 800°C and  
655 1 GPa: Implications for the High Electrical Conductivity Anomalies in Mantle Wedges.  
656 *Journal of Geophysical Research: Solid Earth*, 126(4), e2020JB021343.  
657 <https://doi.org/10.1029/2020JB021343>
- 658 Iwamori, H. (1998). Transportation of H<sub>2</sub>O and melting in subduction zones. *Earth and Planetary*  
659 *Science Letters*, 160(1–2), 65–80. [https://doi.org/10.1016/S0012-821X\(98\)00080-6](https://doi.org/10.1016/S0012-821X(98)00080-6)
- 660 Jung, H., & Karato, S. I. (2001). Water-Induced Fabric Transitions in Olivine. *Science*, 293(5534),  
661 1460–1463. <https://doi.org/10.1126/SCIENCE.1062235>
- 662 Jung, H., Katayama, I., Jiang, Z., Hiraga, T., & Karato, S. (2006). Effect of water and stress on the  
663 lattice–preferred orientation of olivine. *Tectonophysics*, 421, 1–22.  
664 <https://doi.org/10.1016/j.tecto.2006.02.011>
- 665 Jurewicz, S. R., & Jurewicz, A. J. G. (1986). Distribution of apparent angles on random sections  
666 with emphasis on dihedral angle measurements. *Journal of Geophysical Research*, 91(B9),  
667 9277. <https://doi.org/10.1029/jb091ib09p09277>
- 668 Karato, S. I., Jung, H., Katayama, I., & Skemer, P. (2008). Geodynamic Significance of Seismic  
669 Anisotropy of the Upper Mantle: New Insights from Laboratory Studies. *Annual Review of*  
670 *Earth and Planetary Sciences*, 36, 59–95.  
671 <https://doi.org/10.1146/ANNUREV.EARTH.36.031207.124120>
- 672 van Keken, P. E., Hacker, B. R., Syracuse, E. M., & Abers, G. A. (2011). Subduction factory: 4.  
673 Depth-dependent flux of H<sub>2</sub>O from subducting slabs worldwide. *Journal of Geophysical*  
674 *Research*, 116(B1), B01401. <https://doi.org/10.1029/2010JB007922>
- 675 von Bargen, N., & Waff, H. S. (1986). Permeabilities, interfacial areas and curvatures of partially  
676 molten systems: Results of numerical computations of equilibrium microstructures. *Journal*  
677 *of Geophysical Research*, 91(B9), 9261. <https://doi.org/10.1029/JB091IB09P09261>
- 678 Kneller, E. A., van Keken, P. E., Karato, S. I., & Park, J. (2005). B-type olivine fabric in the  
679 mantle wedge: Insights from high-resolution non-Newtonian subduction zone models. *Earth*  
680 *and Planetary Science Letters*, 237(3–4), 781–797.  
681 <https://doi.org/10.1016/J.EPSL.2005.06.049>

- 682 Kneller, E. A., Long, M. D., & van Keken, P. E. (2008). Olivine fabric transitions and shear wave  
683 anisotropy in the Ryukyu subduction system. *Earth and Planetary Science Letters*, 268, 268–  
684 282. <https://doi.org/10.1016/j.epsl.2008.01.004>
- 685 Laporte, D., & Provost, A. (2000). Equilibrium geometry of a fluid phase in a polycrystalline  
686 aggregate with anisotropic surface energies: Dry grain boundaries. *Journal of Geophysical  
687 Research: Solid Earth*, 105(B11), 25937–25953. <https://doi.org/10.1029/2000jb900256>
- 688 Laporte, D., & Watson, E. B. (1995). Experimental and theoretical constraints on melt distribution  
689 in crustal sources: the effect of crystalline anisotropy on melt interconnectivity. *Chemical  
690 Geology*, 124(3–4). [https://doi.org/10.1016/0009-2541\(95\)00052-N](https://doi.org/10.1016/0009-2541(95)00052-N)
- 691 Laporte, D., Rapaille, C. and Provost, A., (1997). Wetting angles, equilibrium melt geometry, and  
692 the permeability threshold of partially molten crustal protoliths. In *Granite: from segregation  
693 of melt to emplacement fabrics*, 31–54. Springer, Dordrecht. [https://doi.org/10.1007/978-94-017-1717-5-3](https://doi.org/10.1007/978-94-<br/>694 017-1717-5-3)
- 695 Liu, X., & Zhao, D. (2017). P-wave anisotropy, mantle wedge flow and olivine fabrics beneath  
696 Japan. *Geophysical Journal International*, 210, 1410–1431.  
697 <https://doi.org/10.1093/GJI/GGX247>
- 698 Liu, X., Matsukage, K.N., Li, Y., Takahashi, E., Suzuki, T., & Xiong, X., (2018). Aqueous Fluid  
699 Connectivity in Subducting Oceanic Crust at the Mantle Transition Zone Conditions. *Journal  
700 of Geophysical Research: Solid Earth*, 123, 6562–6573  
701 <https://doi.org/10.1029/2018JB015973>
- 702 Marquardt, K., Rohrer, G. S., Morales, L., Rybacki, E., Marquardt, H., & Lin, B. (2015). The most  
703 frequent interfaces in olivine aggregates: the GBCD and its importance for grain boundary  
704 related processes. *Contributions to Mineralogy and Petrology*, 170(4), 1–17.  
705 <https://doi.org/10.1007/S00410-015-1193-9>
- 706 Médard, E., McCammon, C. A., Barr, J. A., & Grove, T. L. (2008). Oxygen fugacity, temperature  
707 reproducibility, and H<sub>2</sub>O contents of nominally anhydrous piston–cylinder experiments using  
708 graphite capsules. *American Mineralogist*, 93(11–12), 1838–1844.  
709 <https://doi.org/10.2138/am.2008.2842>
- 710 Mibe, K., Fujii, T., & Yasuda, A. (1998). Connectivity of aqueous fluid in the Earth's upper mantle.  
711 *Geophysical Research Letters*, 25(8), 1233–1236. <https://doi.org/10.1029/98GL00872>
- 712 Mibe, K., Fujii, T., & Yasuda, A. (1999). Control of the location of the volcanic front in island  
713 arcs by aqueous fluid connectivity in the mantle wedge. *Nature*, 401(6750), 259–262.  
714 <https://doi.org/10.1038/45762>
- 715 Pommier, A., & Evans, R. L. (2017). Constraints on fluids in subduction zones from  
716 electromagnetic data. *Geosphere*, 13(4), 1026–1049. <https://doi.org/10.1130/GES01473.1>
- 717 Pommier, A., Kohlstedt, D. L., Hansen, L. N., Mackwell, S., Tasaka, M., Heidelbach, F., &  
718 Leinenweber, K. (2018). Transport properties of olivine grain boundaries from electrical  
719 conductivity experiments. *Contributions to Mineralogy and Petrology*, 173(5), 41.  
720 <https://doi.org/10.1007/s00410-018-1468-z>

- 721 Price, J. D., Wark, D. A., Watson, E. B., & Smith, A. M. (2006). Grain-scale permeabilities of  
722 faceted polycrystalline aggregates. *Geofluids*, 6(4), 302–318. <https://doi.org/10.1111/j.1468-8123.2006.00149.x>
- 723
- 724 Toramaru, A., & Fujii, N. (1986). Connectivity of melt phase in a partially molten peridotite.  
725 *Journal of Geophysical Research: Solid Earth*, 91(B9), 9239–9252.  
726 <https://doi.org/10.1029/JB091IB09P09239>
- 727 Waff, H. S., & Faul, U. H. (1992). Effects of crystalline anisotropy on fluid distribution in  
728 ultramafic partial melts. *Journal of Geophysical Research*, 97(B6), 9003.  
729 <https://doi.org/10.1029/92JB00066>
- 730 Wark, D. A., & Watson, E. B. (2000). Effect of grain size on the distribution and transport of deep–  
731 seated fluids and melts. *Geophysical Research Letters*, 27(14), 2029–2032.  
732 <https://doi.org/10.1029/2000GL011503>
- 733 Watson, E., & Brenan, J. M. (1987). Fluids in the lithosphere, 1. Experimentally-determined  
734 wetting characteristics of CO<sub>2</sub>–H<sub>2</sub>O fluids and their implications for fluid transport, host-rock  
735 physical properties, and fluid inclusion formation. *Earth and Planetary Science Letters*, 85(4),  
736 497–515. [https://doi.org/10.1016/0012-821X\(87\)90144-0](https://doi.org/10.1016/0012-821X(87)90144-0)
- 737 Watson, E., & Lupulescu, A. (1993). Aqueous fluid connectivity and chemical transport in  
738 clinopyroxene-rich rocks. *Earth and Planetary Science Letters*, 117(1–2), 279–294.  
739 [https://doi.org/10.1016/0012-821X\(93\)90133-T](https://doi.org/10.1016/0012-821X(93)90133-T)
- 740 Watson, E., (1999). Lithologic partitioning of fluids and melts. *American Mineralogist*, 84(11–12),  
741 1693–1710. <https://doi.org/10.2138/AM-1999-11-1201>
- 742 Watson, G. W., Oliver, P. M., & Parker, S. C. (1997). Computer simulation of the structure and  
743 stability of forsterite surfaces. *Physics and Chemistry of Minerals*, 25(1), 70–78.  
744 <https://doi.org/10.1007/S002690050088>
- 745 Worzewski, T., Jegen, M., Kopp, H., Brasse, H., & Taylor Castillo, W. (2011). Magnetotelluric  
746 image of the fluid cycle in the Costa Rican subduction zone. *Nature Geoscience*, 4(2), 108–  
747 111. <https://doi.org/10.1038/ngeo1041>
- 748 Yoshino, T., Takei, Y., Wark, D. A., & Watson, E. B. (2005). Grain boundary wetness of texturally  
749 equilibrated rocks, with implications for seismic properties of the upper mantle. *Journal of  
750 Geophysical Research: Solid Earth*, 110(B8), 1–16. <https://doi.org/10.1029/2004JB003544>
- 751 Yoshino, T., Price, J. D., Wark, D. A., & Watson, E. B. (2006). Effect of faceting on pore geometry  
752 in texturally equilibrated rocks: implications for low permeability at low porosity.  
753 *Contributions to Mineralogy and Petrology*, 152(2), 169–186.  
754 <https://doi.org/10.1007/S00410-006-0099-Y>
- 755 Zheng, Y. F., Chen, R. X., Xu, Z., & Zhang, S. B. (2016). The transport of water in subduction  
756 zones. *Science China Earth Sciences*, 59, 651–682. <https://doi.org/10.1007/s11430-015-5258-4>
- 757
- 758